GLOBAL BROADBAND THERMAL EMISSION MAPS OF THE MOON. D. S. McDougall[1], B. T. Greenhagen[2], K.A. Shirley[1], and T.D. Glotch[1] [1]Department of Geosciences, Stony Brook University, Stony Brook, NY 11794-2100, dylan.mcdougall@stonybrook.edu, [2]Johns Hopkins University, Applied Physics Lab, Laurel, MD.

Introduction: Here we generate global emissivity maps of Earth's Moon with LRO Diviner broadband thermal emission data corrected for illumination conditions using a different method from previous work [1,2]. The broadband channels contain spectral information that can inform compositional analyses in combination with the existing Christiansen Feature (CF) dataset [3].

The CF is an emissivity maximum whose position is correlated with the degree of silicate polymerization, which makes it a useful indicator of mineralogy [4]. The Diviner Lunar Radiometer Experiment locates the CF using 3 narrow bands near 8 μm (channels 3-5) [5]. This information has been used to map global silicate mineralogy of the Moon after correcting the data for the effects of low sun (high incidence) angles on the surface radiance [3].

Diviner also acquires observations at four longer wavelength channels (6-9) with broader bandpasses (13-23, 25-41, 50-100, 100-400 μm respectively) that are designed to measure surface temperature [5]. These bandpasses include compositionally diagnostic spectral features such as Reststrahlen bands and transparency features that affect the values measured by Diviner in the long wavelength channels [6]. However, high incidence angle measurements in these channels have significantly lower radiance values than the same materials with noontime illumination [7]. In order to compare the long wavelength channels to the CF data for use in compositional mapping, the long wavelength data must be normalized to equatorial noontime values.

Methods: Similar to previous work [1,2], the radiance values for each orbit and channel are empirically modeled by fitting a cosine function of the form $L(\theta) = a * \cos(b + c * \theta)^d$, where L is radiance, θ is incidence angle, and *a-d* are coefficients. The uncorrected data is then additively shifted according to the cosine fit so that the mean radiance values match those for noontime data. The data is then normalized across incidence angle by a linear function to compensate for the effects of roughness related anisothermality.

To apply the correction globally, 1.5° wide longitudinal strips selected from orbits of representative highlands and mare areas (centered at -127° and -55° respectively) are used to derive coefficients for the functions described above. These coefficients are themselves fit linearly according to latitude, and the latitude-dependent coefficients are used with the original functions to correct 128 pixel per degree gridded data for each orbit.

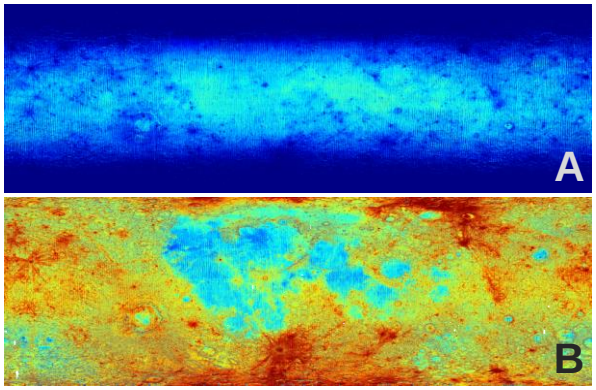

Figure 1A-B: Global maps of the Moon using uncorrected **(A)** and corrected **(B)** Diviner channel 6 (13-23 μm) emissivity stretched from 0.9-1.01 relative to the derived CF emissivity peak value. Latitude is shown between 70°N and 70°S.

After converting to emissivity and finding the median across orbits, the masked images corresponding to the highlands and mare corrections are combined to yield unified global thermal emission maps for each channel.

Deriving empirical fits of radiance and incidence data from a representative region and applying the fits to a global dataset is similar to the LROC WAC empirical photometric correction of [8]. Furthermore, separating corrections for the photometrically distinct lunar mare and highlands regions is precedented by [9]. Unlike these earlier UV-VIS-NIR photometric corrections, the empirical fits used in this work depend only on the cosine of the incidence angle to better represent scattering at thermal wavelengths.

Results and Discussion: High incidence angle, low radiance measurements dominate the uncorrected thermal emission data, especially at latitudes >20° from the equator (Fig. 1A). The high contrast in Fig. 1B demonstrates that the correction has successfully mitigated the effect of high incidence angle measurements for both equatorial and poleward data. The high spatial resolution and applicability of the correction to high latitudes will enable or enhance several analyses that were previously impeded by inaccurate emissivity values for the long wavelength channels, particularly when examining small regions that exhibit spectral anomalies, such as the lunar swirls in Fig. 2.

Some latitude dependence remains in the corrected data due to reemission of reflected thermal radiation onto dark pole-facing slopes. This occurs most

noticeably at high latitudes and for longer wavelength channels. Further modeling may allow correction of this effect, as can modeling of other effects that contribute to unconstrained variation between orbits such as solar distance and orbiter altitude. These corrections would further reduce the remaining striped patterns between spatially adjacent orbits visible in the corrected images.

Correlations with spatially variable surface phenomena in the longitudinal strips of data used to derive empirical fits indicate that the fit equation coefficients likely correspond to physically meaningful values. This relationship also dictates which surface types the fit equations are optimized for when used to correct data for the global maps. The primary relationship is with albedo and coefficient *a*. Coefficients *b*, *c*, and *d* are thought to vary with thermal inertia-related surface properties, as well as the coefficients for the linear anisothermality correction. Per-pixel mapping of these coefficients may be used in the future to derive datasets for surface roughness, regolith fluffiness, or other thermophysical properties that can contribute to the development of existing datsets for these purposes.

Conclusion: The newly corrected data for channels 6 and 7 can be used standalone, with band ratios and indices incorporating the three narrowband short wavelength channels and with calculations using the derived CF position. These methods will help identify non- or extreme silicate mineralogies, develop a correction for the effects of space weathering, and constrain thermophysical properties of surfaces independently of their albedo. After incorporating the latest data and extending the correction to channels 8 and 9, finalized global imagery using the correction will be included in a future LRO Diviner level 4 data product.

Acknowledgements: Much appreciation goes to the JHUAPL SES staff and summer interns for hosting DSM during this work, the Diviner Operations team for collecting data, and NASA for supporting LRO. Funding for this work was provided by the LRO Extended Mission science program and the RIS^{4}E SSERVI team.

References: [1] Shirley K.A. et al. (2016) *LPS XLVII*, #2923 [2] McDougall D.S. et al. (2017) *LPS XLVIII*, #2843 [3] Greenhagen B.T. et al. (2010) *Science* 329, 1507-1509 [4] Greenhagen B.T. and Paige D.A. (2006) *LPSC XXXVII*, #2406 [5] Paige D.A. et al. (2010) *Space Sci. Rev.* 150, 125-160 [6] Salisbury J.W. and Walter L.S. (1989) *JGR*, 94, 9192-9202. [7] Shirley K.A. & Glotch T.D. (2014) *LPS XLV*, #2399. [8] Boyd et al. (2012) *LPS XLIII*, #2795 [9] Hicks et al. (2011) *JGR*, 116, E00G15 [10] Lucey P.G. et al. (2017) *Icarus*, 283, 343-351

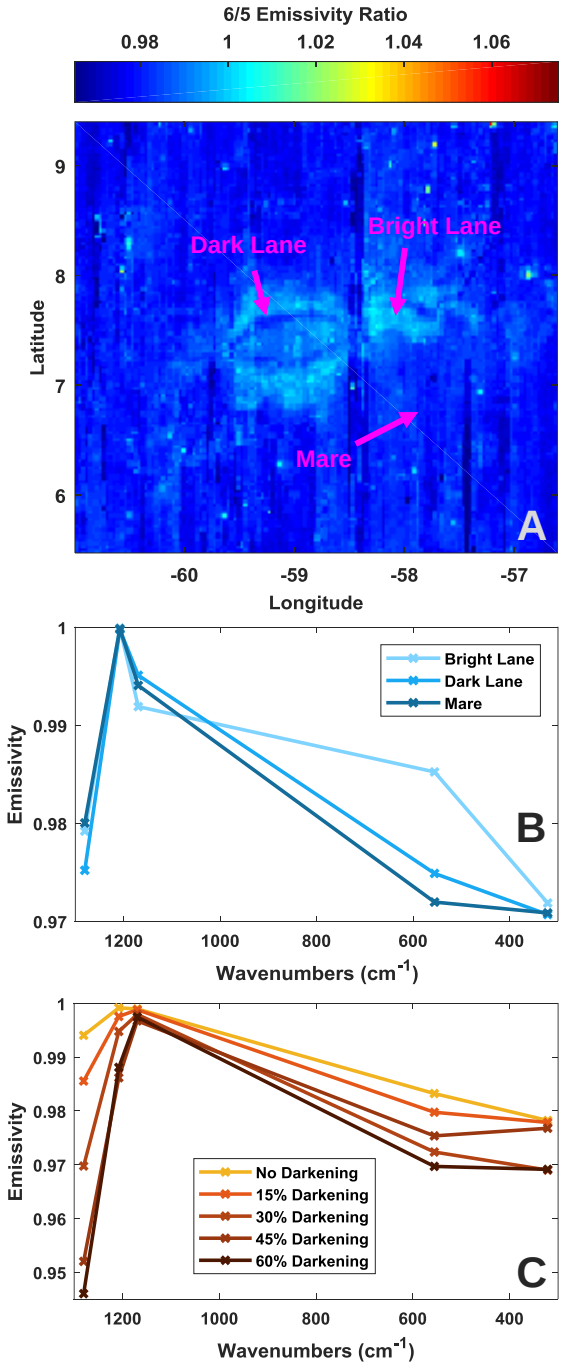

Figure 2A-C: (A) Corrected channel ratio (6/5) image of the Reiner Gamma swirl in Oceanus Procellarum. **(B)** Corrected spectra of regions marked in (A). Bright lanes exhibit anomalously low space weathering relative to the surrounding dark lanes and mare. **(C)** Laboratory spectra of synthetically darkened augite powder in a simulated lunar environment and convolved to Diviner channels 3-7. This darkening is analogous to the space weathering process thought to be occurring in the dark regions surrounding lunar swirls. [10]